A robust method to update local river inundation maps using global climate model output and weather typing based statistical downscaling

M. Bermúdez[1*], L. Cea[2], E. Van Uytven[3], P. Willems[3], J.F. Farfán[2], J. Puertas[2]

[1] *Environmental Fluid Dynamics Group, Andalusian Institute for Earth System Research, University of Granada, Spain*

[2] *Water and Environmental Engineering Group, Department of Civil Engineering, Universidade da Coruña, Spain*

[3] *Department of Civil Engineering – Hydraulics Section, KU Leuven, Belgium*

** Corresponding author: e-mail: mariabermudez@ugr.es, ORCID: 0000-0003-3189-4791*

Abstract

Global warming is changing the magnitude and frequency of extreme precipitation events. This requires updating local rainfall intensity-duration-frequency (IDF) curves and flood hazard maps according to the future climate scenarios. This is, however, far from straightforward, given our limited ability to model the effects of climate change on the temporal and spatial variability of rainfall at small scales. In this study, we develop a robust method to update local IDF relations for sub-daily rainfall extremes using Global Climate Model (GCM) data, and we apply it to a coastal town in NW Spain. First, the relationship between large-scale atmospheric circulation, described by means of Lamb Circulation Type classification (LCT), and rainfall events with potential for flood generation is analyzed. A broad ensemble set of GCM runs is used to identify frequency changes in LCTs, and to assess the occurrence of flood generating events in the future. In a parallel way, we use this Weather Type (WT) classification and climate-flood linkages to downscale rainfall from GCMs, and to determine the IDF curves for the future climate scenarios. A hydrological-hydraulic modeling chain is then used to quantify the changes in flood maps induced by the IDF changes. The results point to a

This version of the article has been accepted for publication, after peer review (when applicable) and is subject to Springer Nature's AM terms of use, but is not the Version of Record and does not reflect post-acceptance improvements, or any corrections. The Version of Record is available online at: https://doi.org/10.1007/s11269-020-02673-7

future increase in rainfall intensity for all rainfall durations, which consequently results in an increased flood hazard in the urban area. While acknowledging the uncertainty in the GCM projections, the results show the need to update IDF standards and flood hazard maps to reflect potential changes in future extreme rainfall intensities.

Keywords: extreme floods; weather types; rainfall variability; climate change; statistical downscaling

Acknowledgments

María Bermúdez acknowledges funding from EU's Horizon 2020 Programme under Marie Skłodowska-Curie Grant Agreement 754446 and UGR Research and Knowledge Transfer Fund—Athenea3i. Els Van Uytven was funded by a doctoral grant from the Research Foundation – Flanders (F.W.O., grant number 11ZY418N)

1. Introduction

Floods are the most common natural hazard worldwide. According to the global EM-DAT database, they represented nearly half of all weather-related disasters in the period 1995-2015 and affected more than 2 billion people (CRED and UNISDR 2015). Changes in storminess associated with global warming can modify the magnitude and frequency of extreme precipitation events (O'Gorman 2015) and exacerbate existing risks. For the 1.5°C temperature rise target, the amount of people exposed to river flooding globally is estimated to increase by 50-60 %, with direct flood damage rising in the range of 160% to 240% (Dottori et al. 2018).

Rainfall Intensity Duration Frequency (IDF) curves form the basis for quantifying extreme precipitation for various durations and return periods for water engineering planning and design. They are commonly used to create synthetic rainfalls that are then used in flood inundation models to obtain flood hazard maps. It is thus crucial that these curves reflect potential changes in future extreme rainfall intensities, as a first step towards obtaining hazard maps representative of future conditions. IDF curves currently in use, based on historical records, may no longer hold under an altered climate regime (Madsen et al. 2009; Peck et al. 2012; Singh et al. 2016).

In this context, climate change projections constitute another approach to historical records to update local IDF curves and flood hazard maps. This is, however, far from straightforward, given our limited ability to model the effects of climate change on the temporal and spatial variability of rainfall at small scales. Global Climate Models (GCMs) are typically run at rather coarse spatial resolutions (above 100 km) and daily time step. Processes that influence local rainfall such as convection operate at smaller scales and are thus not resolved but parameterized in GCMs (Fosser et al. 2015; Tabari et al. 2016). Additionally, local orography and surface characteristics that exert an influence on local rainfall distribution are also poorly represented at these scales (Maraun and Widmann 2015).

This creates a gap between the spatial and temporal scales of the GCM output and those needed to drive local impact models (van den Hurk et al. 2018), which is usually overcome by downscaling

techniques, either statistical or dynamic. A key advantage of statistical downscaling methods is that they are comparatively cheap and computationally efficient (Fowler et al. 2007) to use them with multi-model ensemble predictions, which have become the standard paradigm for the characterization of future changes in hydrological impact studies (Hosseinzadehtalaei et al. 2017). Statistical downscaling methods are generally grouped into three categories (Fowler et al. 2007): (1) regression models which directly translate large atmospheric information to local-scale data (e.g., multiple linear regression, stepwise regression, and artificial neural networks), (2) weather generators, with input parameters modified according to scenarios from a GCM, that replicate the statistical attributes of a local-scale variable, and (3) weather classification schemes that classify the atmospheric circulation at the synoptic scale into a set of weather types (WT) and condition local weather on those large-scale WTs.

All the above statistical approaches rely on the assumption that the relationship established for the present climate will not vary over time (Salvi et al. 2016). From this perspective, methods that yield physically interpretable linkages between the large scale circulation and local surface climate are preferable. This is in fact one of the key advantages of using weather type-based approaches, which provide a greater understanding of the causal mechanisms that lead to weather events (i.e., the large-scale climatic environment associated to a given local weather condition), and provide a more reliable and objective framework for obtaining local projections. Moreover, given the complexity of the relationship between the large-scale flow and local-scale weather, linear models that directly link predictor fields and predictands usually perform worse (Maraun and Widmann 2018).

The link between large-scale climate and local weather events, established by means of WTs, can also be potentially used to directly project future changes in flood occurrence (Hall et al. 2014; Merz et al. 2014). Several studies have analyzed the relationship between precipitation, which could serve as a proxy for flood occurrence, and WTs, and have explored the potential of this relationship to predict precipitation variability (Linderson 2001; Goodess and Jones 2002; Brisson et al. 2011; Cortesi et al. 2013). In regions where a strong link exists, it would be possible to evaluate future changes in WT

frequencies as an indirect means of exploring future flooding. Projections of synoptic weather types under climate change can be obtained almost immediately from the output of GCMs, which are expected to correctly reproduce large scale atmospheric features (Räisänen 2007; Hargreaves 2010; Hargreaves and Annan 2014). A few works have indeed analyzed the ability of GCMs in reproducing circulation patterns, and explored changes in synoptic variability in the 21st century (Demuzere et al. 2009; Lorenzo et al. 2011a; Åström et al. 2016; Otero et al. 2018).

The above strategies based on examining climate-flood connections are regarded as a promising complementary technique to the simulation of the complete flood hazard chain. The latter is currently the most widely used approach that begins with the downscaling of GCMs, followed by hydrological models to evaluate runoff generation. Model chains can also be extended to include hydraulic models for flood routing and inundation analysis, or even damage and loss models (Felder et al. 2018).

In this study, we combine both strategies to develop a robust method to update local flood hazard maps using GCM data. First, the relationship between large-scale atmospheric circulation, described by means of Lamb circulation type classification (LCT) and rainfall events with potential for flood generation in the studied area is analyzed. A broad ensemble set of GCM runs is used to identify frequency changes in LCTs, and to assess the occurrence of flood generating events in the future. In a parallel way, we use this WT classification and climate-flood linkages to downscale rainfall from the GCM climate projections, and determine IDF curves for the future climate. A hydrological-hydraulic modeling chain is then used to quantify the changes in flood discharge and inundation hazard maps induced by climate changes. It should be noted that the comparison between current and future conditions does not account for changes in land use or in initial soil moisture state.

2. Materials and methods

2.1. Study site and rainfall data

The proposed methodology was applied to estimate the impact of future climate change on

precipitation extremes and flood hazard in the coastal town of Betanzos, located in a 440 km^2 basin in the NW of Spain (Figure 1). The Mandeo River and its tributary, the river Mendo, flow through the town and discharge in the estuary of Betanzos (Figure 1). Daily peak discharges measured since 2010 at two gauge stations (one on each catchment) managed by the Regional Water Administration (Augas de Galicia) are available. The urban area of Betanzos is vulnerable to flooding as a result of high precipitation and increased river discharge, and is classified as a high potential flood risk area by the regional authorities. Given its proximity to the sea, existing flood risks in this town could be aggravated not only by changes in precipitation but also through changes in sea levels. However, the scope of this evaluation is limited to the future changes in precipitation and their impact on flood hazard, without considering climate change effects on sea levels.

To characterize the maximum rainfall intensities in the study area, there are 11 rain gauges located around the catchments of the rivers Mandeo and Mendo, operated by the regional meteorological agency MeteoGalicia. The rainfall data registered by these pluviometers at 10-minute time resolution were spatially interpolated using a natural neighbor interpolation, and then averaged over the whole catchment in order to obtain a basin-averaged time series of rainfall. More accurate rainfall interpolation methods, e.g., kriging with external drift (KED), could not be used because radar data is not available for the whole historical period. Nevertheless, as justified in Cea and Fraga (2018), at this study site the difference between natural neighbor and KED interpolation is not relevant for aggregation times larger than 1 hour. The time series of rainfall obtained in this way covers a historical period of 18 years (2001-2018) at 10-minute resolution. Although there are some gaps in the rainfall series of certain stations, the time series of basin-averaged rainfall is complete given the relatively high number of stations used in the interpolation. The average annual maximum 24-hour rainfall depth during the historical period is 49 mm, while the average annual precipitation in the catchment is 1210 mm.

2.2. Classification of atmospheric circulation patterns and link to rainfall events

A large number of WT classification systems have been developed over the last decades (Philipp et al. 2010). Lamb WT classification, with the corresponding objective classification of Jenkinson and Collison (1977), has been prominently applied in mid-high latitudes (Otero et al. 2018). In this study, the Jenkinson Collision modified Lamb weather types (Jenkinson and Collison 1977; Trigo and DaCamara 2000; Philipp et al. 2010) were used to characterize the daily large-scale atmospheric circulation that affects the NW of Spain. It should be noted that the classification of Trigo and DaCamara (2000) was developed to study the precipitation regime in a region very close to the study site of this paper.

The atmospheric classification system considers the sea level pressure in a 16 point grid centred around the case study location (indicated by the rectangle in Figure 1), and calculates flow and vorticity indices. The flow and vorticity indices are compared to define 26 different WTs that are then regrouped into 10 WTs. This regrouping is done by combining all the different cyclonic and anticyclonic WTs into just 2 WTs. Moreover, the hybrid WTs are equally divided over the complementary cyclonic or anticyclonic WT and directional WT (NE, E, SE, S, SW, W, NW and N).

Daily mean sea level pressure (SLP) to calculate historical LCTs frequency was extracted from the ERA Interim dataset (period 1979-2015) (Dee et al. 2011). A set of 123 GCM runs corresponding to the Coupled Model Intercomparison Project CMIP-5 for the four Representative Concentration Pathway (RCP) scenarios was used to assess the future LCTs' occurrence in the period 2071-2100. This far-future period is a common choice for climate change impact analysis, which allows comparability with other studies. The 123 GCM runs encompass 37 runs for RCP8.5, 16 runs for RCP6.0, 41 runs for RCP4.5 and 29 runs for RCP2.6.

The frequency of occurrence of each WT was calculated, and the number of historical storm rainfall events associated with a given WT was evaluated. In addition, the magnitude of the associated 24-hour rainfall was explored for each rainfall event. For this purpose, high-intensity rainfall events were defined from the historical rainfall time series considering storm durations of 1, 3, 6, 12, 18 and 24

hours. For each duration, the high-intensity rainfall events were defined as those with an average rainfall intensity higher than 30% of the average annual maximum rainfall for that specific duration. A minimum one week lag between events was also imposed to avoid statistical dependence, as previously used in Cea and Fraga (2018). These criteria produced 239 independent events in the period 2001-2015 (i.e., around 17 events per year).

2.3. Weather type statistical downscaling method

The downscaled projected precipitation time series were produced using the weather typing based statistical downscaling method SD-B-7 developed by Willems and Vrac (2011). Downscaling by this WT based method is performed in three steps. Firstly, an atmospheric classification system is applied to determine the historical and climate modeled Jenkinson Collision modified Lamb weather types, following the process described in section 2.2. In the second step, an analogue method is applied to the climate model output for the scenario period. More specifically, for each projected wet day in the scenario period (2071-2100), the historical wet day having a similar WT, occurring in the same season and best approximating the exceedance probability of the daily precipitation amount is defined as the analogue day. The projected precipitation time series is constructed by combining the precipitation amount sequences for the analogue days. The case study analyzed in this paper is focused on a small catchment where rainfall duration is typically shorter than a day. For larger catchments, the downscaling could be applied to rainfall events instead of on a day-by-day basis. In the last step of the downscaling process, the projected precipitation time series are rescaled following the Clausius-Clapeyron relation (CC relation). This relation assumes an intensification of extreme precipitation amounts by 7% per degree temperature increase. For each of the projected time series, the CC relation is defined at the annual time scale using the daily hydro-meteorological information. The precipitation scaling is performed using seasonal quantile based average daily temperature changes.

Following the above method, WTs and temperature were used as large-scale predictors, while the local-scale predictand was the daily precipitation accumulation. From the set of 123 GCM runs used

to assess future LCTs' occurrence, a combination of 19 GCMs and 2 RCPs (i.e., a total of 38 GCM runs) was chosen to obtain projected precipitation time series based on data availability (required variables available from all 19 GCMs, and GCM projections available for both RCP scenarios).

2.4. Estimation of IDF curves and synthetic hyetographs

IDF curves for the study catchment were estimated from the historical and projected basin-averaged precipitation time series. Using basin-averaged time series to evaluate the IDF curves avoids the need to apply generic Areal Reduction Factors (ARF) derived for other catchments or regions (Wright et al. 2014; Cea and Fraga 2018).

The basin-averaged time series of historical and projected rainfall were aggregated at durations of 1, 3, 6, 12, 18 and 24 hours, obtaining thus six rainfall time series for each climate condition (historical, RCP 4.5 and RCP 8.5), each one with a different aggregation time step. Each register of the time series was classified according to its corresponding WT, and the annual maximum rainfall depth was obtained for each aggregation duration and WT. The exceedance probability of the sampled data was estimated using the formula of Gringorten (1963). A two-parameter Gumbel extreme value distribution was fitted to the data. The choice of the Gumbel distribution instead of the Generalized Extreme Value (GEV) distribution was made considering the relatively short length of the available time series (18 years). This was also the reason why the IDF curves were only computed for return periods up to 50 years. In this way, IDF relations were developed for each WT separately and then composed into a single IDF curve by summing for all WT the product of their distribution function and their probability of occurrence. This was done for the historical precipitation data and for the future precipitation series obtained from each of the 38 GCMs runs corresponding to the RCP 4.5 and RCP 8.5. Thus, 19 IDFs were computed for each future climate scenario (one IDF per GCM run).

The basin-averaged IDF curves were used to build synthetic design hyetographs for different return periods (T=2, 10, 25 and 50 years) and climate conditions (historical, RCP 4.5 and RCP 8.5). For that purpose, the median of the 19 IDFs available for each future climate scenario was used to characterize

each RCP. The synthetic hyetographs were built with the Alternating Block Method using a block duration of 1 hour. This is short enough compared to the estimated concentration time of the catchments (about 10 hours). In whole 12 synthetic design hyetographs were obtained as the combination of 4 return periods and 3 climate conditions.

2.5. Hydrological and hydraulic models

The semi-distributed model HEC-HMS v4.2.1 (Scharffenberg and Fleming 2006) and its geospatial toolkit HEC-GeoHMS (Fleming and Doan 2009) were used to transform the synthetic hyetographs in flood hydrographs. The Mandeo (353 km^2) and Mendo (84 km^2) basins were subdivided into 34 and 24 subbasins, respectively, with areas ranging from 0.2 to 30 km^2. Effective rainfall was estimated using the SCS curve number method. A curve number (CN) corresponding to average antecedent soil moisture conditions (AMC) was assigned to each subbasin according to its Hydrological Soil-Cover Complex (soil cover, practice, hydrological condition, and hydrological soil group). The SCS unit hydrograph was used to model rainfall-runoff transformation, using the TR55 method (USDA Soil Conservation Service 1986) to compute the concentration time (Tc) of each subbasin, and the relation Tlag= 0.6 Tc to estimate the lag time (Tlag). Flow routing in the river stream network was modelled with the kinematic wave approximation. More specific details on the hydrological model can be found in Cea and Fraga (2018).

The 12 synthetic design hyetographs were introduced in the HEC-HMS model to compute the corresponding flood hydrographs, which were then used as boundary conditions in a two-dimensional hydrodynamic model to obtain the inundation hazard maps in the urban area of Betanzos for each climate condition and return period. The inundation model is based on the software Iber+ (Bladé et al. 2014; García-Feal et al. 2018), which solves the 2D depth-averaged shallow water equations with an unstructured finite volume solver. The model has been extensively validated and applied to river inundation studies (Garrote et al. 2016; Bermúdez et al. 2017; Sopelana et al. 2018; Areu-Rangel et al. 2019). Figure 1 shows the extension and topography of the numerical model, which includes the city

of Betanzos (at the confluence of the rivers Mandeo and Mendo) and extends up to the ocean in order to correctly impose the tidal condition. The computational grid has about 126000 elements, with a mesh size of the order of 5 m in the urban area. In the outer estuary the grid size increases to 50 m, which is enough to correctly propagate the tidal wave from the ocean to the urban area. The topography of the model was interpolated from a high-accuracy digital elevation model with a spatial resolution of 1 m (much finer than the mesh size). The only parameter of the model is the Manning bed roughness coefficient, which was specified considering six different land-use types. The flood hydrographs were imposed in the model as upstream boundary conditions, whereas the tidal level was imposed at the open sea boundary (Figure 1). Since the study aims to evaluate the impact of increased extreme rainfall on flood hazard maps, a semi-diurnal tidal wave with a period of 12.42 hours and an average tidal range of 2.5 m was used as the open sea boundary condition in all the inundation simulations.

3. Results and discussion

3.1. Relationship between atmospheric circulation and precipitation events

From the analysis of the historical 36-year series of daily WTs (1979-2015), it can be observed that the anticyclone type (A in Figure 2), with high pressures over the studied area, is dominant throughout the year and reaches its higher frequency during the summer months. Cyclone type (C in Figure 2), associated with low pressures, also occurs consistently throughout the year, but its relative frequency is much lower, particularly in summer. Directional types N and NE show a seasonal behavior opposite to W and SW types, with maxima from April to September in the former case and from October to March in the latter. NW and E exhibit a similar frequency of occurrence throughout the year. The weather types with the lowest relative frequencies are directional types S and SE. These observations are consistent with the analysis of atmospheric circulation patterns performed by (Lorenzo et al. 2008) in the same region, using a different reanalysis dataset and period of analysis.

The analysis of high rainfall events and WT frequencies showed that the majority of intense

precipitation events in the catchment are associated with weather types W, SW and C (Figure 3a). The overall number of high rainfall events occurring in winter (Oct-Mar) is higher than in summer months (Apr-Sep) (138 vs. 101 events) (Figure 3a), and its average magnitude is also higher (Figure 3c). In winter, SW and W types, characterized by low-pressure systems over the North Atlantic, explain more rain events than C types. By contrast, C is the WT with the highest occurrence of high rainfall events in summer. Very few rainfall events occur during NE, E, SE and S types, characterized by high pressures over the British Isles, regardless of the season. Weather types C, W and SW alone explain 80% of all winter rainfall events and 60% of the summer ones. In addition, NE, E and SE rainfall events produce low rainfall magnitudes (Figure 3b).

3.2. Future changes in WT frequencies

Future LCTs frequency was extracted from daily sea-level pressure projections from GCMs, as explained in section 2.2. Prior to conducting this analysis, the capability of the selected GCMs to reproduce current LCT frequencies was verified using the control runs (1961-1990). The comparison between the results obtained from the GCMs and those obtained from the historical reanalysis data are shown in Figure S1 of the supplementary materials. The main discrepancies were found for westerly and anticyclonic types. The overestimation in the W frequency and underestimation of A frequency are well-known biases in the synoptic circulation simulated by GCMs in some regions (Addor et al. 2016; Otero et al. 2018). Overall, a reasonably good agreement was found.

Changes in frequency between the respective control runs (1961-1990) and the future period simulations (2071-2100) from the GCMs are shown in Figure 4 for the WTs linked to high rainfall events (i.e., C, W and SW). The future LCTs estimated from the different GCM runs show a large spread in the frequency changes. The median predictions show a decrease in the C types throughout the year, and a slight increase of SW and W types in winter. For most of the seasons and LCTs, changes are stronger for higher RCP scenarios.

The link between the above weather types and high rainfall events shown in Figure 3a suggests that

there could be an increase in winter high rainfall events, which are usually associated with W and SW types. By contrast, the number of high rainfall events occurring in summer could decrease, since they are associated with C followed by W types, and both WTs are predicted to decrease in summer. These results corroborate the findings of Lorenzo et al. (2011b), indicating a decrease in the future frequency of C, W and SW circulation types in the spring and summer months. Given that Lorenzo et al. (2011b) used only three GCMs (CMIP-3 simulations), our work presented in this paper constitutes an updated analysis (CMIP-5 simulations) with a larger set of GCMs that provides insight into the uncertainties involved.

In spite of the relationship that exists between WTs and high rainfall events, it is obvious that WTs cannot be used alone as a proxy for rainfall occurrence. Other factors operating at smaller time and space scales than synoptic-scale phenomena explain the occurrence of high rainfall. It is, however, an indirect means of gaining insight into the future rainfall change as a result of the synoptic variability changes, which are better simulated by GCMs than rainfall projections.

3.3. IDF curves for different climate conditions

The basin-averaged IDF curves computed for the historical and RCP 8.5 climate scenario are shown in Figure 5. The IDF curves estimated from the RCP 4.5 projections can be found in the Supplementary Materials (Figure S2). In the case of the RCP 8.5 scenario, the IDF computed from the 19 GCMs, as well as its median value, are shown in order to give a visual estimation of the variability of the downscaled GCMs projections. Figure 5 shows an increase in maximum rainfall intensity for all the return periods and rainfall durations. Moreover, all the GCMs predict an increase in maximum rainfall intensities, even though the ratio between projected and historical IDFs varies widely from one GCM to another.

The increase in the RCP 8.5 median IDF compared to the historical IDF is almost 25 % for rainfall durations smaller than 12 hours, which are the most relevant in the catchments of NW Spain, given their relatively small size. The ratio between RCP 8.5 and historical IDFs diminishes as the rainfall

duration increases, being almost negligible for a 48-hour rainfall. The most extreme rainfall projections give maximum differences up to 50 % relative to the historical IDF, while the softer projections predict an increase in maximum rainfall intensities lower than 10% (Figure 5).

It should be noticed when analyzing these results that any methodology that is driven by input from GCMs is dependent on the GCM skill in predicting the variables that form that input, in our case rainfall intensity. This limitation is shared by all downscaling techniques, including the more complex dynamic downscaling, which is dependent on boundary conditions obtained from GCMs.

3.4. Flood hydrographs

The basin-averaged IDF curves presented in Figure 5 were used to build synthetic design hyetographs using the Alternating Block Method. Those hyetographs were then transformed to design flood hydrographs for both the Mandeo and Mendo rivers using the HEC-HMS hydrological model. In whole, 12 hyetographs and 24 flood hydrographs were computed, which correspond to the 4 return periods and the 3 climate conditions represented in Figure 6. In the case of RCP 4.5 and RCP 8.5, the median IDF was used to build the synthetic hyetographs. The first thing that stands out is the relative increase in peak discharges, which is much larger than the increase in the peak rainfall intensities. This is because the differences in the peak of effective precipitation between climate conditions are much larger than the differences in total precipitation, even if the same values of CN were used in all the hydrological simulations. Even so, since the volume of the projected hyetographs is larger than the volume of the historical hyetographs, the infiltration capacity of the soil when the maximum rainfall intensity occurs is lower for the RCP 4.5 and 8.5 scenarios, producing much higher peaks of streamflow.

Compared to the historical flood hydrograph, the peak discharge computed for the RCP 4.5 is between 1.32 and 1.49 times higher, depending on the return period (please refer to supplementary materials - Table S1). Higher relative increments of runoff are obtained for the lower return periods. The same trend is observed for the RCP 8.5, although in this case the relative increment on peak

discharge varies from 1.61 (for T=50 years) to 1.85 (for T=2 years). It is interesting to notice when comparing the historical and future climate conditions in Table S1 that the relative increase in the peak discharge is similar to the relative increase in the peak of effective precipitation intensity (except for T=2), and higher than the relative increase in the effective precipitation depth. This effect can also be observed in the hydrographs presented in Figure 6, where it is clearly shown that the relative difference in the peak of the hydrographs is higher than the difference in volume. Moreover, Table S1 shows that the differences between historical and future climate conditions are highly amplified when comparing peak discharges instead of total rainfall, even if potential future changes in land use and antecedent soil moisture conditions have not been considered in this analysis, in which the same values of CN have been used in all the hydrological simulations.

3.5. Flood maps

In this section, we estimate the extent and magnitude of flooding for the different climate conditions. The increased rainfall and runoff for future scenarios result in an increased flood extent in the urban area compared with current estimates for the same return period (Figure 7a). For the T=2 years storm event, the model results show that water stays in-bank in the historical conditions. However, in future scenarios, both the river Mandeo and Mendo overflow their banks in the upstream areas of the model domain for this return period. The flood extent is larger for RCP8.5 than RCP4.5, representing an increase from historical conditions of 60 % and 20 %, respectively (please refer to supplementary materials - Table S2).

The flood extent obviously increases with higher return periods (Figure 7a). The water completely covers the floodplain for the design storm of T=25 years in the historical scenario. In future scenarios, this situation is expected to occur more frequently, and as low as T=10 years in RCP8.5. Comparatively, the relative increase in flood extent with respect to historical conditions is lower for the higher return periods (Table S2). The reason behind this is that the floodplains are constrained by the steep slopes of the surrounding terrain. Therefore, lateral flood expansion is limited and flood

extent for all design storms with a return period above 25 years (i.e., once the floodplain is inundated in the historical conditions) is very similar.

For the higher return period events, the differences between the different simulations are mainly reflected in depth changes. The depth difference (90^{th} percentile) with respect to historical conditions reaches 1.4 m for RCP8.5 and 0.71 m for RCP4.5 (Table S2). If these differences are plotted spatially (Figure 7b), it can be seen that the largest differences are located in the upstream part of the River Mandeo, because of the narrow width of this floodplain in this area. The spatial distribution of maximum depth differences is very similar between scenarios RC4.5 and RCP8.5 (please refer to Figure S2 in the supplementary materials for RCP4.5 results), but the magnitude of the differences is significantly higher for RCP8.5. The maximum depth differences with respect to historical simulations occur for T=50 years, and reach up to 1.69 m for RCP4.5 and 2.34 m for RCP8.5.

Inundation levels in this coastal town are driven mainly by the river discharge. However, it is also important to be aware that, for low-return period discharges, sea level can also be responsible for high water surface elevations in the areas closer to the estuary (Sopelana et al. 2018; Bermúdez et al. 2019b). In this work, the average tide representative of normal conditions is imposed, so the potential role played by high sea levels on inundation levels is not considered. Future changes in mean sea level due to global warming are also not considered. Another important aspect regarding the limitations of the calculated flood maps is that they rely on the median IDF of all GCM runs. The calculation of flood maps using the individual IDF curves developed for each GCM run would be very computer-intensive for a detailed physically-based hydraulic model like the one used here, and would probably require the development of a fast surrogate model (Bermúdez et al. 2019a).

4. Conclusions

In this study, we developed a robust method to update local flood hazard maps using Global Climate Model (GCM) data. The LCT classification proved to be a valuable tool to analyze possible changes in the probability of occurrence of high rainfall events and to generate local-scale rainfall projections

in the studied area. The median of the future climate IDF curves, calculated from all the downscaled GCMs, show an increase in rainfall intensity for all studied rainfall durations. For durations below 12 h, which are the most relevant in the studied area due to the small catchment size, the increase in maximum rainfall intensity in RCP 8.5 median IDF is almost 25% compared to the historical IDF. The differences between historical and future climate conditions are highly amplified when comparing peak discharges instead of total rainfall (future peak discharges are between 1.32 and 1.85 times higher than in the historical hydrographs, depending on the RCP and return period considered).

The results show that existing IDF standards and flood maps need to be updated to reflect potential changes in future extreme rainfall intensities. Although the results presented use the best available information concerning future climate change, huge uncertainties remain. Therefore, besides updating IDF relations and flood maps, engineering design guidelines that incorporate climate change need to ensure that no regret solutions are being taken, and flexibility/adaptability to adjust to the uncertain future conditions.

A limitation of the methodology is that it does not account for potential changes in initial soil moisture conditions between present and future climate. There is no straightforward way to ascertain these potential changes in soil moisture in an event-based hydrological- hydraulic modelling approach like the one proposed here. To overcome this limitation, an alternative approach based on running a continuous mode hydrological model with future climate data could be considered. Future work should also consider potential changes in other sources of flooding (e.g., mean sea level rise associated with global warming) in regions with compound flooding potential.

Conflict of Interest

None

References

Addor N, Rohrer M, Furrer R, Seibert J (2016) Propagation of biases in climate models from the

synoptic to the regional scale: Implications for bias adjustment. J Geophys Res Atmos 121:2075–2089. doi: 10.1002/2015JD024040

Areu-Rangel O, Cea L, Bonasia R, Espinosa-Echavarria V (2019) Impact of Urban Growth and Changes in Land Use on River Flood Hazard in Villahermosa, Tabasco (Mexico). Water 11:304. doi: 10.3390/w11020304

Åström HLA, Sunyer M, Madsen H, et al (2016) Explanatory analysis of the relationship between atmospheric circulation and occurrence of flood-generating events in a coastal city. Hydrol Process 30:2773–2788. doi: 10.1002/hyp.10767

Bermúdez M, Cea L, Puertas J (2019a) A rapid flood inundation model for hazard mapping based on least squares support vector machine regression. J Flood Risk Manag e12522. doi: 10.1111/jfr3.12522

Bermúdez M, Cea L, Sopelana J (2019b) Quantifying the role of individual flood drivers and their correlations in flooding of coastal river reaches. Stoch Environ Res Risk Assess 33:1851–1861. doi: 10.1007/s00477-019-01733-8

Bermúdez M, Neal JC, Bates PD, et al (2017) Quantifying local rainfall dynamics and uncertain boundary conditions into a nested regional-local flood modeling system. Water Resour Res 53:2770–2785. doi: 10.1002/2016WR019903

Bladé E, Cea L, Corestein G, et al (2014) Revista Internacional de Métodos Numéricos para Cálculo y Diseño en Ingeniería Iber: herramienta de simulación numérica del flujo en ríos Iber — River modelling simulation tool. Rev Int Mètodos Numèricos para Cálculo y Diseño en Ing 30:1–10. doi: 10.1016/j.rimni.2012.07.004

Brisson E, Demuzere M, Kwakernaak B, Van Lipzig NPM (2011) Relations between atmospheric circulation and precipitation in Belgium. Meteorol Atmos Phys 111:27–39. doi:

10.1007/s00703-010-0103-y

Cea L, Fraga I (2018) Incorporating Antecedent Moisture Conditions and Intraevent Variability of Rainfall on Flood Frequency Analysis in Poorly Gauged Basins. Water Resour Res 54:8774–8791. doi: 10.1029/2018WR023194

Cortesi N, Trigo RM, Gonzalez-Hidalgo JC, Ramos AM (2013) Modelling monthly precipitation with circulation weather types for a dense network of stations over Iberia. Hydrol Earth Syst Sci 17:665–678. doi: 10.5194/hess-17-665-2013

CRED, UNISDR (2015) The human cost of weather related disasters 1995-2015

Dee DP, Uppala SM, Simmons AJ, et al (2011) The ERA-Interim reanalysis: configuration and performance of the data assimilation system. Q J R Meteorol Soc 137:553–597. doi: 10.1002/qj.828

Demuzere M, Werner M, van Lipzig NPM, Roeckner E (2009) An analysis of present and future ECHAM5 pressure fields using a classification of circulation patterns. Int J Climatol 29:1796–1810. doi: 10.1002/joc.1821

Dottori F, Szewczyk W, Ciscar J-C, et al (2018) Increased human and economic losses from river flooding with anthropogenic warming. Nat Clim Chang 8:781–786. doi: 10.1038/s41558-018-0257-z

Felder G, Gómez-Navarro JJ, Zischg AP, et al (2018) From global circulation to local flood loss: Coupling models across the scales. Sci Total Environ 635:1225–1239. doi: 10.1016/J.SCITOTENV.2018.04.170

Fleming MJ, Doan JH (2009) HEC-GeoHMS Geospatial Hydrologic Modeling Extension

Fosser G, Khodayar S, Berg P (2015) Benefit of convection permitting climate model simulations in the representation of convective precipitation. Clim Dyn 44:45–60. doi: 10.1007/s00382-014-

2242-1

Fowler HJ, Blenkinsop S, Tebaldi C (2007) Linking climate change modelling to impacts studies: recent advances in downscaling techniques for hydrological modelling. Int J Climatol 27:1547–1578. doi: 10.1002/joc.1556

García-Feal O, González-Cao J, Gómez-Gesteira M, et al (2018) An Accelerated Tool for Flood Modelling Based on Iber. Water 10:1459. doi: 10.3390/w10101459

Garrote J, Alvarenga FM, Díez-Herrero A (2016) Quantification of flash flood economic risk using ultra-detailed stage-damage functions and 2-D hydraulic models. J Hydrol 541:611–625. doi: 10.1016/j.jhydrol.2016.02.006

Goodess CM, Jones PD (2002) Links between circulation and changes in the characteristics of Iberian rainfall. Int J Climatol 22:1593–1615. doi: 10.1002/joc.810

Gringorten II (1963) A plotting rule for extreme probability paper. J Geophys Res 68:813–814. doi: 10.1029/JZ068i003p00813

Hall J, Arheimer B, Borga M, et al (2014) Understanding flood regime changes in Europe: a state-of-the-art assessment. Hydrol Earth Syst Sci 18:2735–2772. doi: 10.5194/hess-18-2735-2014

Hargreaves JC (2010) Skill and uncertainty in climate models. Wiley Interdiscip Rev Clim Chang 1:556–564. doi: 10.1002/wcc.58

Hargreaves JC, Annan JD (2014) Can we trust climate models? Wiley Interdiscip Rev Clim Chang 5:435–440. doi: 10.1002/wcc.288

Hosseinzadehtalaei P, Tabari H, Willems P (2017) Uncertainty assessment for climate change impact on intense precipitation: how many model runs do we need? Int J Climatol 37:1105–1117. doi: 10.1002/joc.5069

Jenkinson AF, Collison F. (1977) An initial climatology of gales over the North Sea

Linderson M-L (2001) Objective classification of atmospheric circulation over southern Scandinavia. Int J Climatol 21:155–169. doi: 10.1002/joc.604

Lorenzo MN, Ramos AM, Taboada JJ, et al (2011a) Changes in Present and Future Circulation Types Frequency in Northwest Iberian Peninsula. PLoS One 6:. doi: 10.1371/journal.pone.0016201

Lorenzo MN, Ramos AM, Taboada JJ, Gimeno L (2011b) Changes in Present and Future Circulation Types Frequency in Northwest Iberian Peninsula. PLoS One 6:e16201. doi: 10.1371/journal.pone.0016201

Lorenzo MN, Taboada JJ, Gimeno L (2008) Links between circulation weather types and teleconnection patterns and their influence on precipitation patterns in Galicia (NW Spain). Int J Climatol 28:1493–1505. doi: 10.1002/joc.1646

Madsen H, Arnbjerg-Nielsen K, Mikkelsen PS (2009) Update of regional intensity–duration–frequency curves in Denmark: Tendency towards increased storm intensities. Atmos Res 92:343–349. doi: 10.1016/J.ATMOSRES.2009.01.013

Maraun D, Widmann M (2015) The representation of location by a regional climate model in complex terrain. Hydrol Earth Syst Sci 19:3449–3456. doi: 10.5194/hess-19-3449-2015

Maraun D, Widmann M (Martin L (2018) Statistical downscaling and bias correction for climate research. Cambridge University Press

Merz B, Aerts J, Arnbjerg-Nielsen K, et al (2014) Floods and climate: emerging perspectives for flood risk assessment and management. Nat Hazards Earth Syst Sci 14:1921–1942. doi: 10.5194/nhess-14-1921-2014

O'Gorman PA (2015) Precipitation Extremes Under Climate Change. Curr. Clim. Chang. Reports

1:49–59

Otero N, Sillmann J, Butler T (2018) Assessment of an extended version of the Jenkinson–Collison classification on CMIP5 models over Europe. Clim Dyn 50:1559–1579. doi: 10.1007/s00382-017-3705-y

Peck A, Prodanovic P, Simonovic SPP (2012) Rainfall Intensity Duration Frequency Curves Under Climate Change: City of London, Ontario, Canada. Can Water Resour J / Rev Can des ressources hydriques 37:177–189. doi: 10.4296/cwrj2011-935

Philipp A, Bartholy J, Erpicum M, et al (2010) Cost733cat – A database of weather and circulation type classifications. Phys Chem Earth, Parts A/B/C 35:360–373. doi: 10.1016/J.PCE.2009.12.010

Räisänen J (2007) How reliable are climate models? Tellus, Ser. A Dyn. Meteorol. Oceanogr. 59:2–29

Salvi K, Ghosh S, Ganguly AR (2016) Credibility of statistical downscaling under nonstationary climate. Clim Dyn 46:1991–2023. doi: 10.1007/s00382-015-2688-9

Scaife AA, Woollings T, Knight J, et al (2010) Atmospheric Blocking and Mean Biases in Climate Models. J Clim 23:6143–6152. doi: 10.1175/2010JCLI3728.1

Scharffenberg WA, Fleming MJ (2006) Hydrologic Modeling System HEC-HMS: User's Manual

Singh R, Arya DS, Taxak AK, Vojinovic Z (2016) Potential Impact of Climate Change on Rainfall Intensity-Duration-Frequency Curves in Roorkee, India. Water Resour Manag 30:4603–4616. doi: 10.1007/s11269-016-1441-4

Sopelana J, Cea L, Ruano S (2018) A continuous simulation approach for the estimation of extreme flood inundation in coastal river reaches affected by meso- and macrotides. Nat Hazards 93:1337–1358. doi: 10.1007/s11069-018-3360-6

Tabari H, De Troch R, Giot O, et al (2016) Local impact analysis of climate change on precipitation extremes: are high-resolution climate models needed for realistic simulations? Hydrol Earth Syst Sci 20:3843–3857. doi: 10.5194/hess-20-3843-2016

Trigo RM, DaCamara CC (2000) Circulation weather types and their influence on the precipitation regime in Portugal. Int J Climatol 20:1559–1581. doi: 10.1002/1097-0088(20001115)20:13<1559::AID-JOC555>3.0.CO;2-5

USDA Soil Conservation Service (1986) Technical Release 55: Urban Hydrology for Small Watersheds

van den Hurk B, Hewitt C, Jacob D, et al (2018) The match between climate services demands and Earth System Models supplies. Clim Serv 12:59–63. doi: 10.1016/J.CLISER.2018.11.002

Willems P, Vrac M (2011) Statistical precipitation downscaling for small-scale hydrological impact investigations of climate change. J Hydrol 402:193–205. doi: 10.1016/j.jhydrol.2011.02.030

Wright DB, Smith JA, Baeck ML (2014) Critical Examination of Area Reduction Factors. J Hydrol Eng 19:769–776. doi: 10.1061/(ASCE)HE.1943-5584.0000855

FIGURES

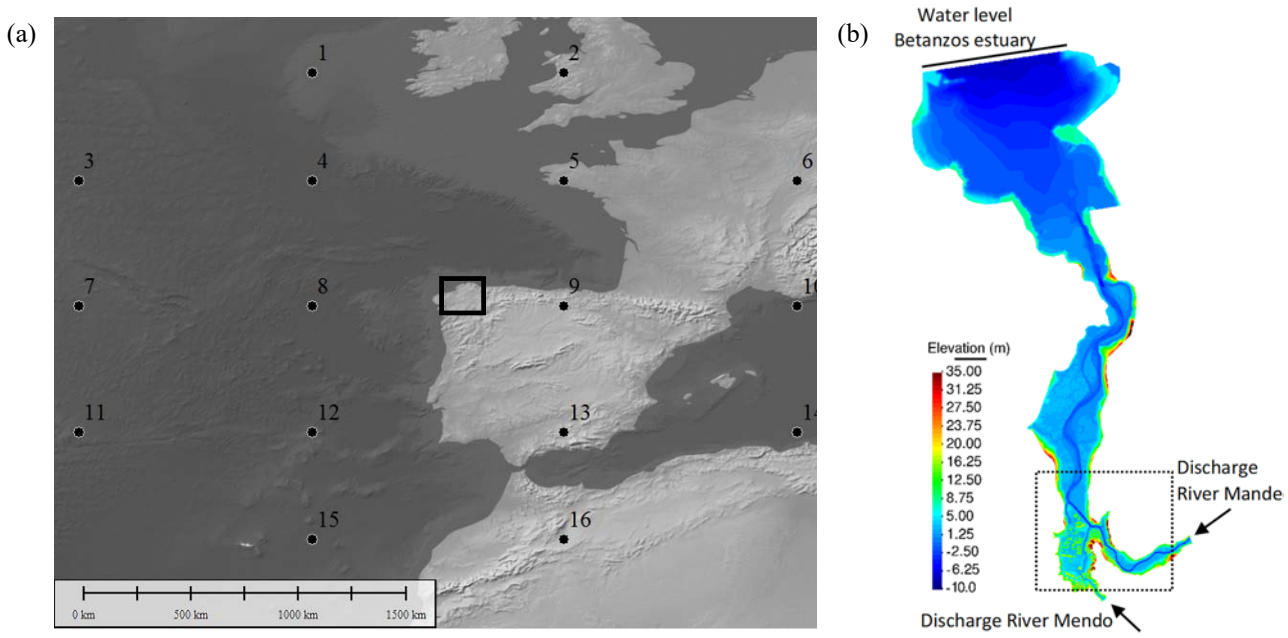

Fig. 1 (a) Location of the case study site (marked with a rectangle) and grid points for the calculation of WTs (1 to 16) (left). **(b)** Topography used in the flood inundation model with the location of the open boundaries and the urban area of Betanzos (dashed rectangle).

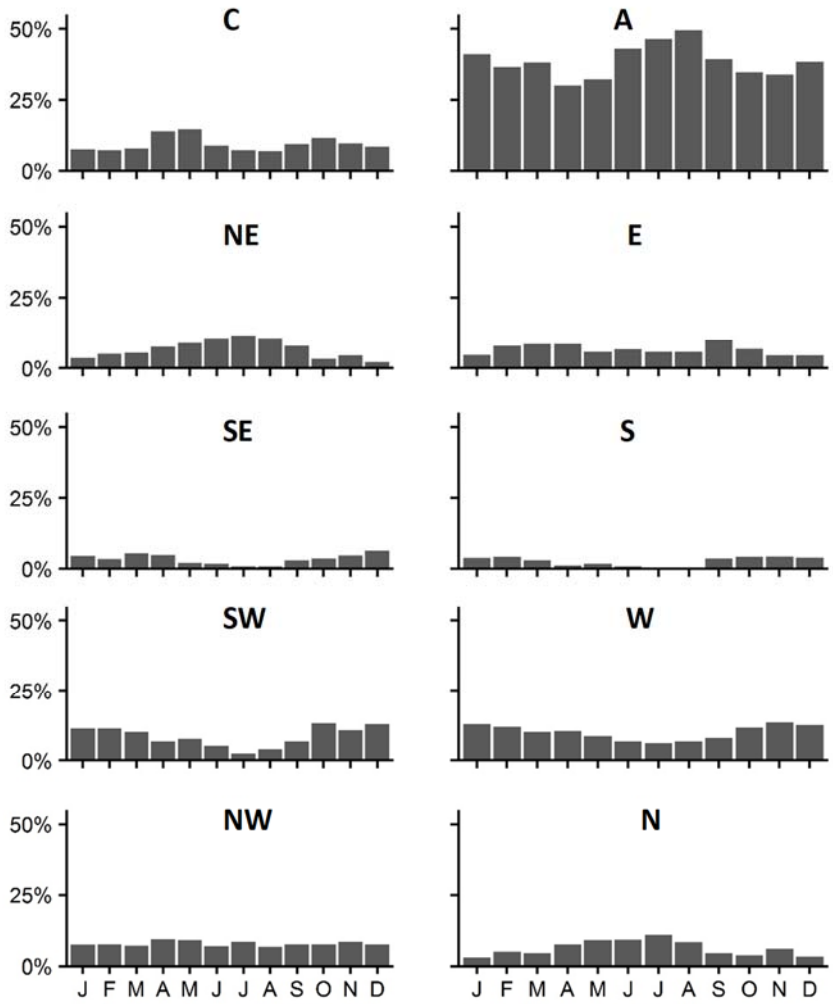

Fig. 2 Mean monthly relative frequency of the synoptic weather type based on the ERA Interim dataset (period 1979-2015). Note: Cyclonic (C), anticyclonic (A) and directional weather types (NE, E, SE, S, SW, W, NW, N).

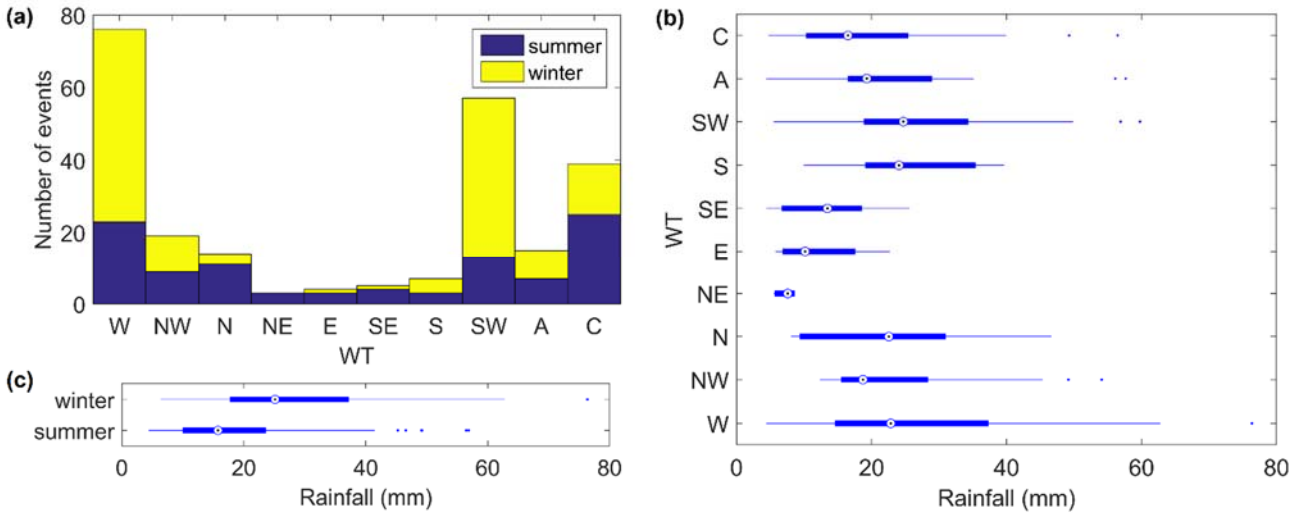

Fig. 3 (a) Absolute frequency of high rainfall events per weather type and season, based on data of 14 years (2001-2015), **(b)** Magnitude of accumulated daily rainfall per weather type in those events (both seasons), and **(c)** Magnitude of accumulated daily rainfall per season in those events. In the box and whisker plots, the central mark is the median, the box edges are the first and third quartile, the whiskers (lines) extend to the most extreme point within 1.5 times the interquartile range, and outliers are plotted as points beyond the whiskers.

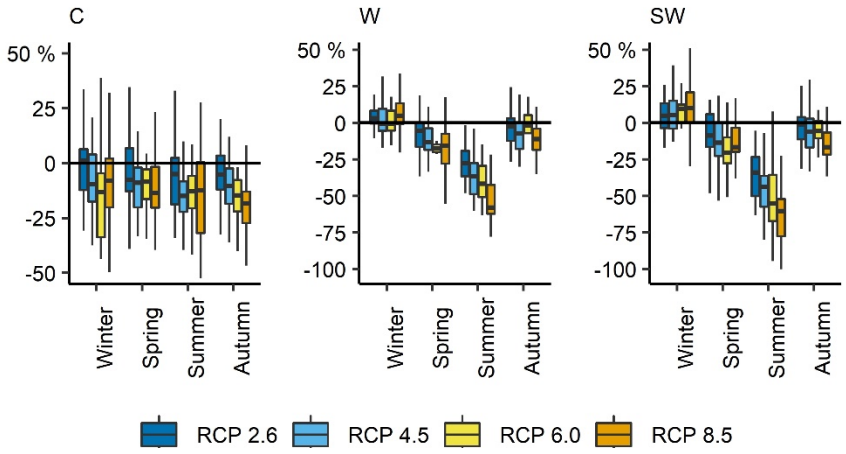

Fig 4. Seasonal changes in the WT frequency of C, W and SW type for each of the four RCP scenarios, compared with the historical period. The box edges indicate the first and third quartile, the central mark in the box is the median and the whiskers (lines) extend to the 5th and 95th percentiles.

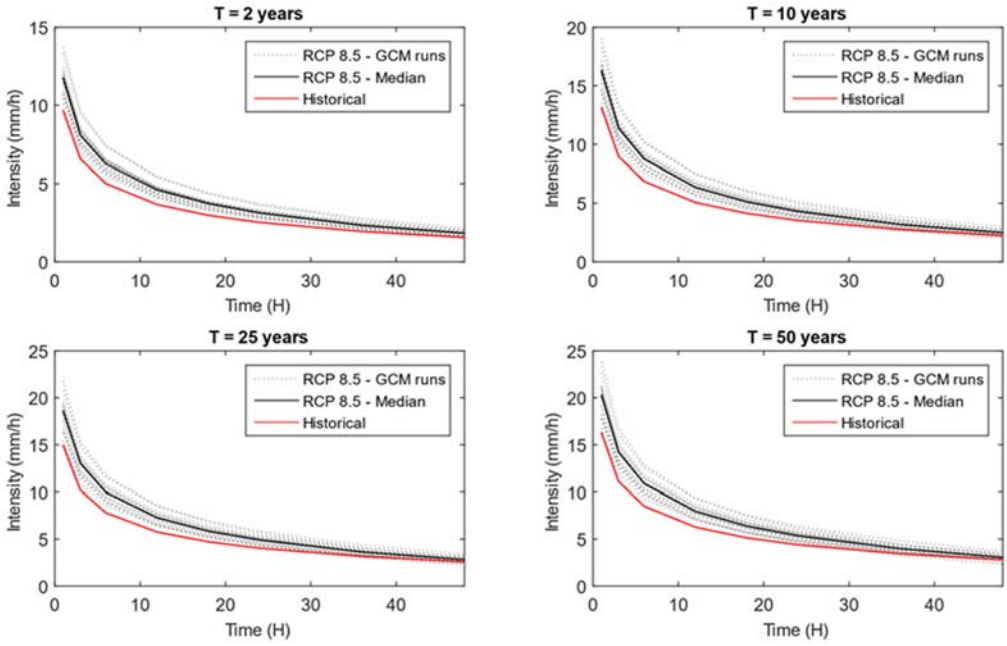

Fig. 5 Basin-averaged IDF curves estimated from the historical rainfall and from the RCP 8.5 projected rainfall time series, for different return periods (2, 10, 25 and 50 years). The IDFs computed with all the GCM projections for the RCP 8.5 climate scenario are shown in addition to its median value.

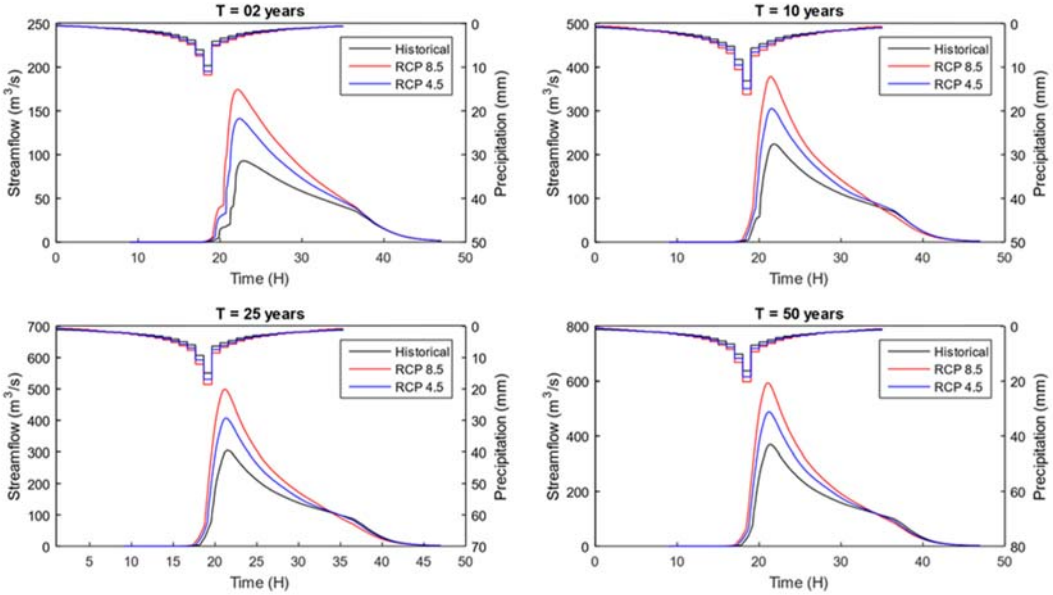

Fig 6. Design synthetic hyetographs and hydrographs fo the different climate conditions (historical, RCP 4.5 and RCP 8.5) and return periods (2, 10, 25 and 50 years). The hydrographs shown correspond to the Mandeo river.

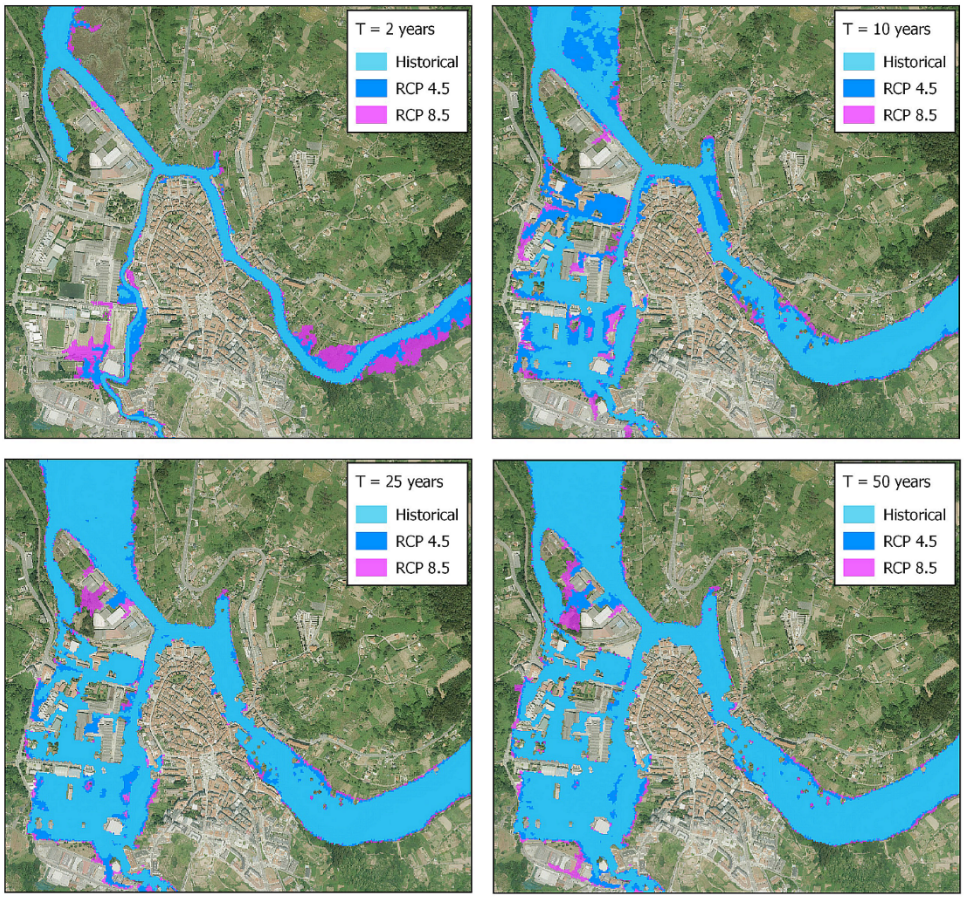

(a) Flood extent

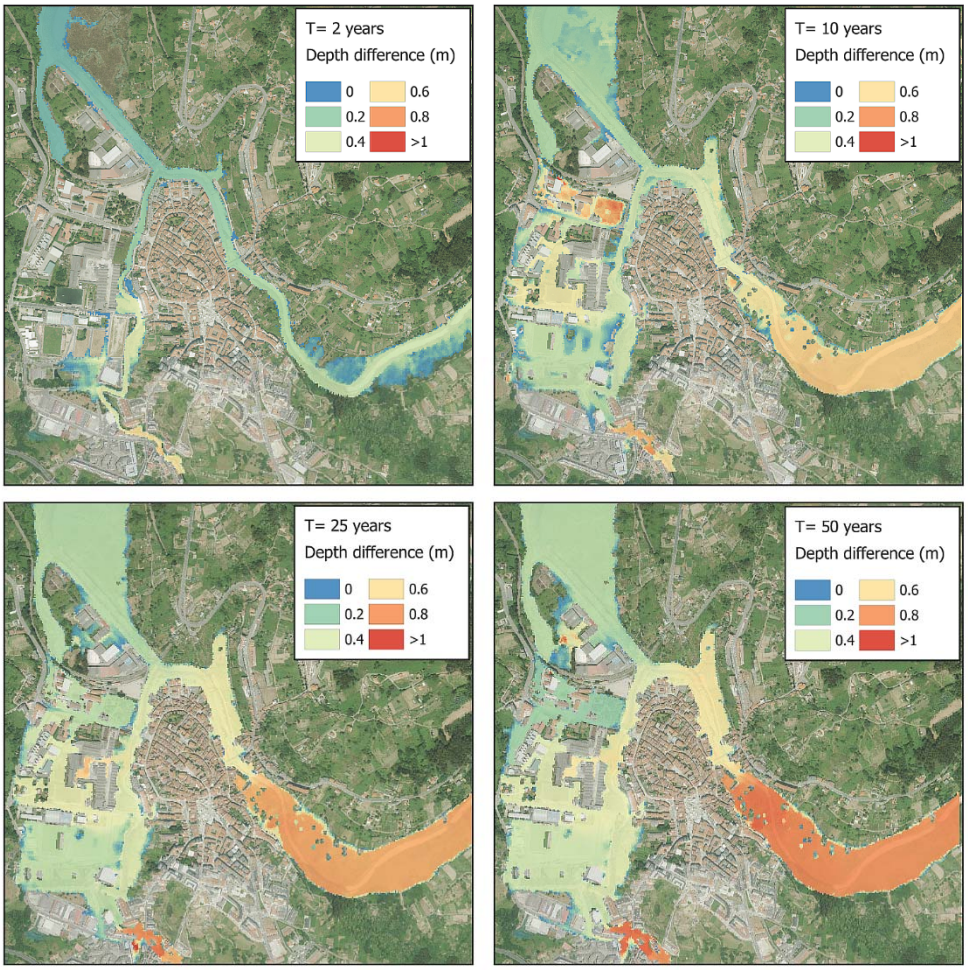

(b) Depth difference

Fig. 7 (a) Estimated maximum flood extent for the different scenarios. **(b)** Difference in flood depth between future scenario RCP8.5 and historical conditions for the different return periods analyzed. The figure only shows the urban area of Betanzos.

SUPPLEMENTARY MATERIALS

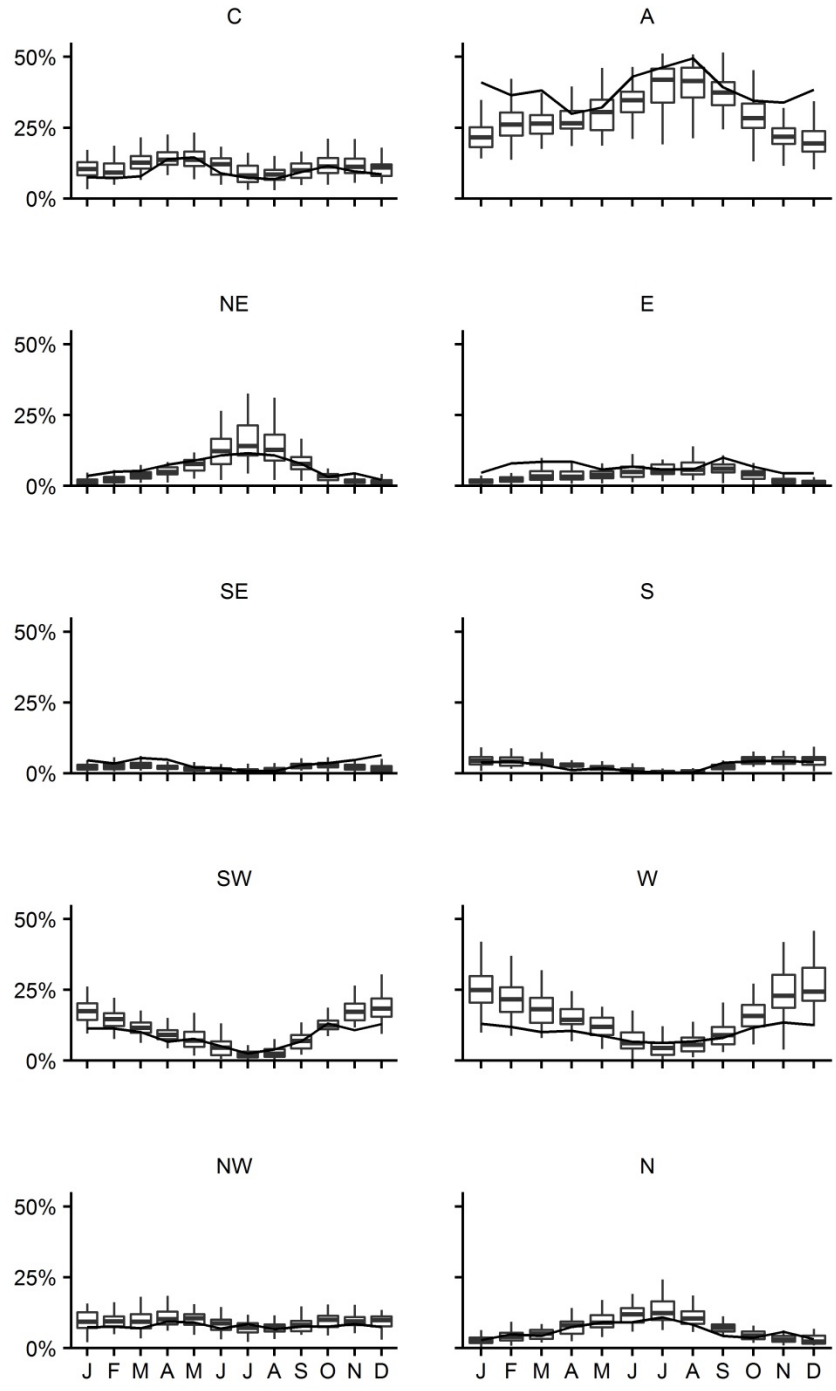

Fig. S1 Monthly frequency bias of the WT classification based on GCM, where the boxplots are the weather type frequencies for the control runs of the GCMs (1961-1990) and the continuous lines are the weather type frequencies based on the ERA Interim dataset (1979-2015).

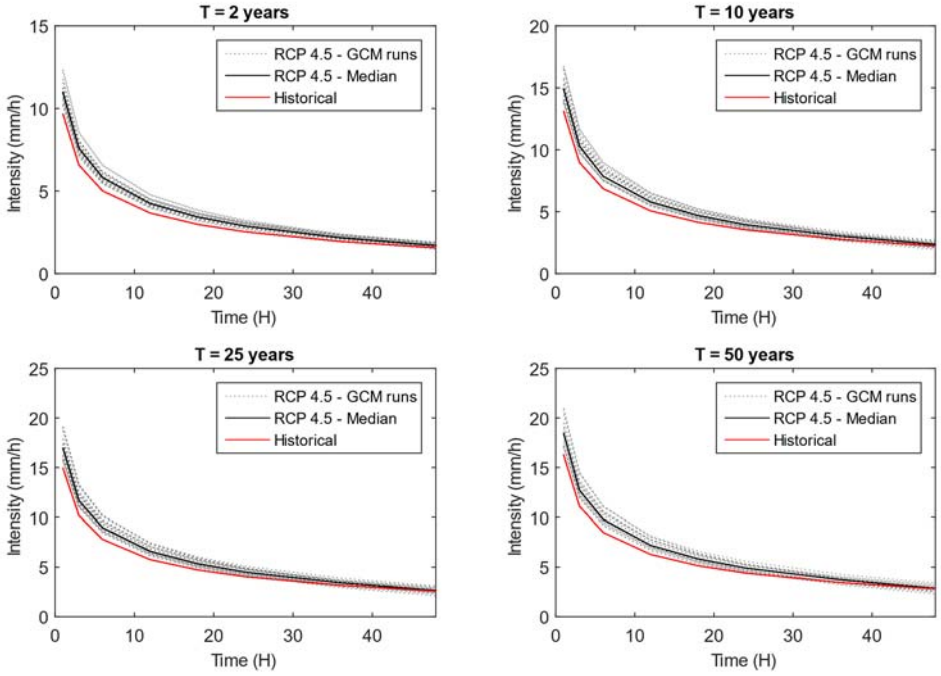

Fig S2. Basin-averaged IDF curves estimated from the historical rainfall and from the RCP 4.5 projected rainfall time series, for different return periods (2, 10, 25 and 50 years). The IDFs computed with all the GCM projections are shown in addition to its median value.

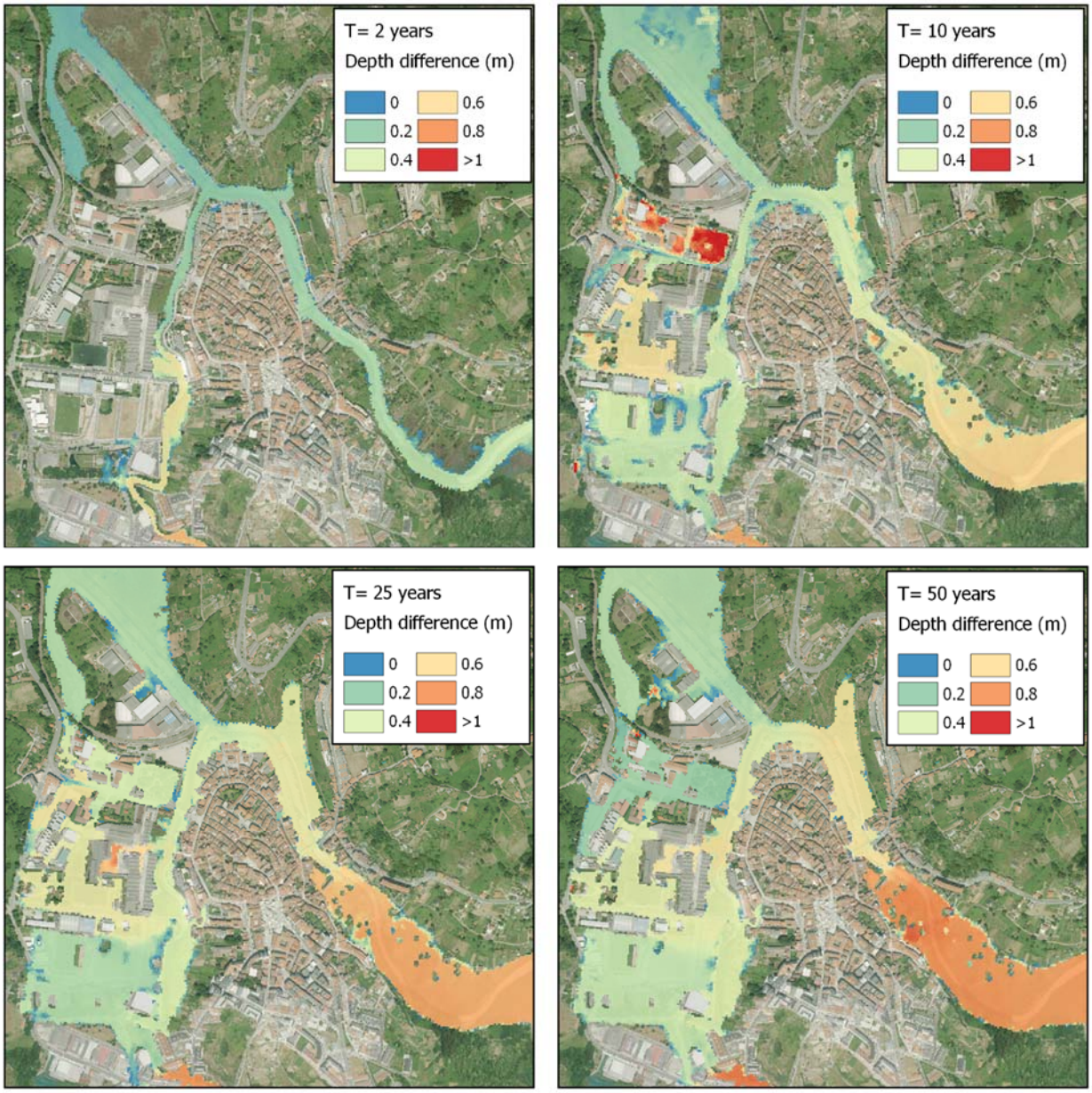

Fig. S3. Differences in flood depth between future scenario RCP4.5 and historical conditions for the different return periods analyzed.

Table S1. Characteristic values of the synthetic hyetographs and flood hydrographs for the Mandeo river computed for the historical, RCP 4.5 and RCP 8.5 scenarios.

Return period (years)		Total rainfall intensity peak (mm/h)	Effective rainfall depth (mm)	Effective rainfall intensity peak (mm/h)	Peak discharge (m3/s)
	Historical	9.7	10.9	1.2	82.9
	RCP 4.5	11.0	14.9	2.0	123.2
T=2	RCP 8.5	11.7	18.0	2.6	153.0
	Ratio RCP 4.5	**1.13**	**1.37**	**1.72**	**1.49**
	Ratio RCP 8.5	**1.22**	**1.65**	**2.22**	**1.85**
	Historical	13.1	24.5	3.5	192.9
	RCP 4.5	14.9	30.7	4.9	264.1
T=10	RCP 8.5	16.3	35.3	6.0	327.7
	Ratio RCP 4.5	**1.14**	**1.25**	**1.38**	**1.37**
	Ratio RCP 8.5	**1.24**	**1.44**	**1.69**	**1.70**
	Historical	14.9	32.6	4.9	263.2
	RCP 4.5	16.9	39.7	6.6	351.2
T=25	RCP 8.5	18.6	45.6	8.0	426.3
	Ratio RCP 4.5	**1.13**	**1.22**	**1.33**	**1.33**
	Ratio RCP 8.5	**1.24**	**1.40**	**1.61**	**1.62**
	Historical	16.3	38.6	6.0	318.4
	RCP 4.5	18.4	46.7	7.9	418.8
T=50	RCP 8.5	20.3	53.7	9.5	513.4
	Ratio RCP 4.5	**1.13**	**1.21**	**1.31**	**1.32**
	Ratio RCP 8.5	**1.25**	**1.39**	**1.58**	**1.61**

Table S2. Values of the metrics used to compare extent and magnitude of flooding for the different climate conditions.

Return period (years)	Flooded area (ha)			Ratio of flooded area against historical		Mean depth difference with historical (m)		P90 depth difference with historical (m)	
	Historical	RCP 4.5	RCP 8.5	RCP 4.5	RCP 8.5	RCP 4.5	RCP 8.5	RCP 4.5	RCP 8.5
T=2	19.5	23.6	30.8	1.210	1.580	0.26	0.39	0.48	0.66
T=10	45.7	62.3	68.0	1.365	1.489	0.40	0.89	0.62	1.13
T=25	62.2	69.8	74.3	1.123	1.195	0.44	0.77	0.72	1.30
T=50	67.5	73.7	78.4	1.092	1.161	0.46	0.82	0.77	1.40